FAST CONVERGENCE AND ASYMPTOTIC PRESERVING OF THE GENERAL SYNTHETIC ITERATIVE SCHEME*

WEI SU†, LIANHUA ZHU‡, AND LEI WU§

Abstract. Recently the general synthetic iteration scheme (GSIS) was proposed for the Boltzmann equation [W. Su et al., *J. Comput. Phys.,* 407 (2020), 109245], where various numerical simulations have shown that (i) the steady-state solution can be found within dozens of iterations at any Knudsen number K, and (ii) the solution is accurate even when the spatial cell size in the bulk region is much larger than the molecular mean free path, i.e., the Navier–Stokes solutions are recovered at coarse grids. The first property indicates that the error decay rate between two consecutive iterations decreases to zero along with K, while the second one implies that the GSIS asymptotically preserves the Navier–Stokes limit when K approaches zero. This paper is first dedicated to the rigorous proof of both properties. Second, several numerically challenging cases (especially the two-dimensional thermal edge flow) are used to further demonstrate the accuracy and efficiency of GSIS.

Key words. gas kinetic equation, false/superconvergence, asymptotic Navier–Stokes preserving

AMS subject classifications. 76P05, 65L04, 65M12

DOI. 10.1137/20M132691X

1. Introduction. Rarefied gas flows are encountered in many engineering problems, including space vehicle re-entry, microelectromechanical system processing, and shale gas extraction. Although several macroscopic equations have been proposed [4, 8, 17], they only work when the Knudsen number K, defined as the ratio of the molecular mean free path to the characteristic system length, is small. To describe the rarefied gas dynamics from the continuum to free molecular flow regimes, the Boltzmann equation from gas kinetic theory is needed. However, it is a grand challenge to solve the Boltzmann equation, as the numerical scheme should be carefully designed, especially when the Boltzmann collision operator becomes stiff at small Knudsen numbers. For example, the direct simulation Monte Carlo method [3] requires the numerical scale (i.e., the spatial cell size Δx and time step Δt) to be smaller than the corresponding kinetic scale (i.e., the mean free path and mean collision time of gas molecules); otherwise, the numerical dissipation will lead to inaccurate solutions. This would become prohibitive in multiscale simulations involving the near-continuum flow where the Knudsen number is small.

Many efforts have been devoted to solving the Boltzmann equation or its simplified model equations under a numerical scale larger than the kinetic one [15, 6, 7, 5, 12, 28, 9]. The common feature of these numerical methods is that they are time dependent. Some schemes asymptotically preserve the Euler limit, i.e., they become consistent discretizations of Euler equations when K goes to zero [6, 7], while some

†School of Engineering, The University of Edinburgh, Edinburgh EH9 3FB, UK (wei.su@ed.ac.uk).
‡James Weir Fluids Laboratory, Department of Mechanical and Aerospace Engineering, University of Strathclyde, Glasgow G1 1XJ, UK (l.zhu@strath.ac.uk).
§Department of Mechanics and Aerospace Engineering, Southern University of Science and Technology, Shenzhen 518055, China (wul@sustech.edu.cn).

asymptotically preserve the Navier–Stokes limit when Δt is much larger than the mean collision time [5, 12] or when both Δt and Δx are much larger than the corresponding kinetic scales [28, 9, 10].

It should be noted that in continuum flows the turbulence is common, and time-dependent numerical solvers for the Navier–Stokes equations are in high demand. However, in rarefied gas dynamics the turbulence is usually absent, and steady-state solutions are of particular interest. Therefore, an implicit solver is strongly recommended, especially in multiscale problems where the Knudsen layer (a few mean free paths away from the solid surface) must be resolved; see the thermal edge flow in section 5.4 for an example. In these cases the time-dependent solver needs a time step at the order of mean collision time, which requires a tremendous number of iteration steps to find the steady-state solution. In designing the implicit solver, one has to consider the following two major problems: (i) how to find the steady-state solution quickly, and (ii) how to recover the solution of the Navier–Stokes equations in the continuum flow regime on coarse spatial grids that are adequate for capturing the hydrodynamics but much larger than the mean free path of gas molecules.

A simple way to obtain the steady-state solution of gas kinetic equations is to use the conventional iterative scheme (CIS), where the collision operator is split into the gain term and the loss term, while the time derivative is dropped. The streaming operator and loss term are calculated at the current iteration step, while the gain term is evaluated at the previous iteration step. Therefore, the resultant ordinary differential equation (ODE) can be effectively solved by the sweep technique after discretization in physical space, without involving the inversion of a large-scale matrix [11]. When the Knudsen number is large, the CIS is efficient since the converged solution can be obtained within a few iterations. Also, it is accurate since the spatial grid size is comparable to the molecular mean free path. However, the iteration number increases significantly when K is small. Moreover, the CIS does not asymptotically preserve the Navier–Stokes limit, so a huge number of spatial cells is required to capture the flow dynamics when K is small [25].

It is noted that the two major deficiencies of CIS not only appear in the gas system but also in other kinetic systems, e.g., for neutron transport, thermal radiation, and phonon transport in crystals (to name just a few). The exciting breakthrough for tackling these deficiencies was first achieved in neutron transport, where the diffusion synthetic acceleration (DSA) was developed; see the review [1]. In DSA, the mesoscopic kinetic equation is solved together with a diffusion equation for the macroscopic variable appearing in the gain part of the collision operator. This diffusion equation is exactly the limiting equation derived from the kinetic equation in optical thick regions (or, equivalently, when K is small) [14]. Not only is fast convergence to the steady state achieved but also asymptotic preserving is accomplished on coarse physical grids in the whole range of the Knudsen number.

The DSA scheme has been extended to some special rarefied gas flows, such as the Poiseuille and Couette flows [24, 27, 19], where the flow velocity appearing in the collision operator is perpendicular to the computational domain, and thus the macroscopic governing equation of flow velocity is an inhomogeneous diffusion equation. In the continuum flow regime the inhomogeneous term vanishes, and the macroscopic equations are reduced to the diffusion equation, while in rarefied flow regimes the inhomogeneous term dominates and captures the rarefaction effects exactly. However, for general rarefied gas flows, the limiting macroscopic equation is not the diffusion equation but rather the Navier–Stokes equations according to the Chapman–Enskog expansion [4]. Thus, in a recent paper we proposed the general synthetic iterative

scheme (GSIS), where the macroscopic synthetic equations take the form of linearized Navier–Stokes equations but with source terms describing high-order rarefaction effects exactly [22], without any truncation as adopted in the moment closure [8].

Since the synthetic equations contain the continuity equation (obtained from mass conservation) that is not of diffusion type, GSIS may exhibit different behaviors compared to other DSA schemes. Although the numerical examples in [22] have shown that GSIS has fast convergence to the steady-state solution and is asymptotic Navier–Stokes preserving, the mathematical proof is lacking. It is therefore the major aim of this paper to rigorously investigate these two properties.

The remainder of this paper is organized as follows. In sections 2 and 3 the convergence rates of CIS and GSIS for the linearized Bhatnagar–Gross–Krook (BGK) kinetic equation [2] are calculated, respectively. The reason for explicitly including the Newton's law of shear stress and the Fourier's law of heat conduction in the macroscopic synthetic equations is analyzed. In section 4 the asymptotic preserving property of GSIS is studied, and it is found that the GSIS preserves the Navier–Stokes limit with $\Delta x \sim O(1)$, as long as this spatial resolution is adequate for capturing the hydrodynamic behavior. In section 5, several numerical simulations, including the most challenging simulation of two-dimensional thermal edge flow in the near-continuum regime, are performed to demonstrate the fast convergence and asymptotic Navier–Stokes preserving properties of the GSIS. A summary is given in section 6.

2. The convergence rate of CIS and false convergence. To make the mathematical derivation simple but keep the essential flow physics, we consider the linearized BGK equation in general two-dimensional problems,

$$(2.1) \qquad \boldsymbol{v} \cdot \frac{\partial h(\boldsymbol{x}, \boldsymbol{v})}{\partial \boldsymbol{x}} = \frac{h_{eq}(\boldsymbol{x}, \boldsymbol{v}) - h(\boldsymbol{x}, \boldsymbol{v})}{K},$$

where $h(\boldsymbol{x}, \boldsymbol{v})$ is the velocity distribution function at location $\boldsymbol{x} = (x_1, x_2)$, $\boldsymbol{v} = (v_1, v_2) \in \mathbb{R}^2$ is the molecular velocity, K is the Knudsen number, and h_{eq} is the reference velocity distribution function,

$$(2.2) \qquad h_{eq}(\boldsymbol{x}, \boldsymbol{v}) = \varrho(\boldsymbol{x}) + 2\boldsymbol{u}(\boldsymbol{x}) \cdot \boldsymbol{v} + \tau(\boldsymbol{x}) \left(v^2 - 1 \right),$$

with ϱ, $\boldsymbol{u} = (u_1, u_2)$, and τ being the density, flow velocity, and temperature deviating from the global equilibrium state, respectively. They are related to the velocity distribution function h as

$$(2.3) \qquad M(\boldsymbol{x}) = [\varrho, u_1, u_2, \tau] = \int m h(\boldsymbol{x}, \boldsymbol{v}) E(\boldsymbol{v}) d\boldsymbol{v},$$

where $E(\boldsymbol{v}) = \exp(-v^2)/\pi$ is the velocity distribution function at global equilibrium, and $m = [1, v_1, v_2, v^2 - 1]$ are the collisional invariants. Also, the shear stress σ_{ij} (with $i, j = 1, 2$) and heat flux q_i are defined as

$$(2.4) \qquad \sigma_{ij}(\boldsymbol{x}) = 2 \int \left(v_i v_j - \frac{v^2}{2} \delta_{ij} \right) h(\boldsymbol{x}, \boldsymbol{v}) E(\boldsymbol{v}) d\boldsymbol{v},$$

$$(2.5) \qquad q_i(\boldsymbol{x}) = \int v_i \left(v^2 - 2 \right) h(\boldsymbol{x}, \boldsymbol{v}) E(\boldsymbol{v}) d\boldsymbol{v},$$

with δ_{ij} the Kronecker delta.

In CIS, given the value of the velocity distribution function $h^{(k)}(\boldsymbol{x}, \boldsymbol{v})$ at the kth iteration step, its value at the next iteration step is calculated by solving the equation

$$(2.6) \qquad h^{(k+1)} + K\boldsymbol{v} \cdot \frac{\partial h^{(k+1)}}{\partial \boldsymbol{x}} = h_{eq}(h^{(k)}),$$

and the process is repeated until the maximum relative difference between successive estimates of the macroscopic quantities, e.g.,

$$(2.7) \qquad \epsilon = \max \left\{ \sqrt{\frac{\int |M^{(k+1)} - M^{(k)}|^2 \mathrm{d}\boldsymbol{x}}{\int |M^{(k+1)}|^2 \mathrm{d}\boldsymbol{x}}} \right\},$$

is less than a preassigned value.

Although in practical numerical simulations the streaming operator $\partial/\partial\boldsymbol{x}$ is discretized, e.g., by the finite-difference, finite-volume, or discontinuous Galerkin (DG) method [21, 20], here it is kept intact when calculating the convergence rate of iteration; that of the discretized version of (2.6) will be tested in numerical simulations in section 5.

To calculate the convergence rate, we first define the following error function between the velocity distribution functions at two consecutive iteration steps,

$$(2.8) \qquad Y^{(k+1)}(\boldsymbol{x}, \boldsymbol{v}) = h^{(k+1)}(\boldsymbol{x}, \boldsymbol{v}) - h^{(k)}(\boldsymbol{x}, \boldsymbol{v}),$$

where, according to (2.6), the error function $Y^{(k+1)}(\boldsymbol{x}, \boldsymbol{v})$ is found to satisfy

$$(2.9) \qquad Y^{(k+1)} + K\boldsymbol{v} \cdot \frac{\partial Y^{(k+1)}}{\partial \boldsymbol{x}} = \Phi_\varrho^{(k)} + 2\Phi_{u_1}^{(k)} v_1 + 2\Phi_{u_2}^{(k)} v_2 + \Phi_\tau^{(k)} \left(v^2 - 1\right),$$

with the following error functions for the macroscopic quantities between two consecutive iteration steps:

$$(2.10) \qquad \Phi_M^{(k+1)}(\boldsymbol{x}) = M^{(k+1)}(\boldsymbol{x}) - M^{(k)}(\boldsymbol{x}) = \int m Y^{(k+1)}(\boldsymbol{x}, \boldsymbol{v}) E(\boldsymbol{v}) d\boldsymbol{v}.$$

Second, to determine the convergence rate ω, we perform the Fourier stability analysis by seeking the eigenvalue ω and eigenfunctions $y(\boldsymbol{v})$ and $\alpha_M = [\alpha_\varrho, \alpha_{u_1}, \alpha_{u_2}, \alpha_\tau]$ of the forms

$$(2.11) \qquad Y^{(k+1)}(\boldsymbol{x}, \boldsymbol{v}) = \omega^k y(\boldsymbol{v}) \exp(i\boldsymbol{\theta} \cdot \boldsymbol{x}),$$

$$(2.12) \qquad \Phi_M^{(k+1)}(\boldsymbol{x}) = \omega^{k+1} \alpha_M \exp(i\boldsymbol{\theta} \cdot \boldsymbol{x}),$$

where i is the imaginary unit, and $\boldsymbol{\theta} = (\theta_1, \theta_2)$ is the wave vector of perturbation. It should be noted that the factor ω^k emerges in (2.11) rather than the factor ω^{k+1} in (2.12) because from (2.9) we know that $Y^{(k+1)}$ is determined by macroscopic quantities in the kth iteration step. Obviously, when ω is very close to zero, the iteration converges quickly. When ω is very close to one, the error between two consecutive steps rarely decreases, so the iteration converges extremely slowly. When $|\omega| > 1$, the iteration will be unstable.

Substituting (2.11) and (2.12) into (2.9) and (2.10), we obtain the following expression for $y(\boldsymbol{v})$:

$$(2.13) \qquad y(\boldsymbol{v}) = \frac{\alpha_\varrho + 2\alpha_{u_1} v_1 + 2\alpha_{u_2} v_2 + \alpha_\tau (v^2 - 1)}{1 + iK\boldsymbol{\theta} \cdot \boldsymbol{v}}.$$
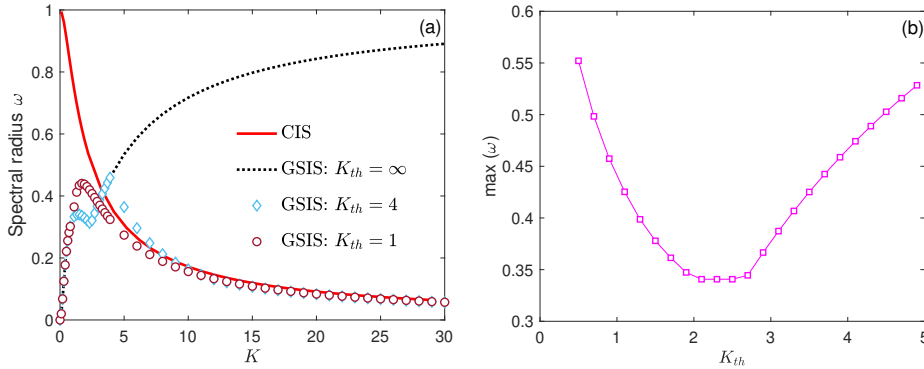
FIG. 1. (a) *The spectral radius ω as a function of the Knudsen number K in both CIS and GSIS. Note that K_{th} is a threshold Knudsen number, which is used to define the correction coefficient β; see (3.23) and (3.2). (b) The maximum spectral radius ω in the whole range of the Knudsen number as a function of K_{th}.*

In the following we assume the wave vector of perturbation satisfies $|\boldsymbol{\theta}|^2 = \theta_1^2 + \theta_2^2 = 1$. Although in reality the perturbation may have various values of $\boldsymbol{\theta}$, their corresponding convergence rates do not interact because the kinetic equation is linear. Moreover, from the denominator in (2.13), we see that the convergence rate depends only on the product of $K\boldsymbol{\theta}$. If $|\boldsymbol{\theta}| \neq 1$, the convergence rate at specific values of $\boldsymbol{\theta}$ and K can be calculated by replacing the Knudsen number with $K|\boldsymbol{\theta}|$.

Finally, with (2.10), (2.11), (2.12), and (2.13), we obtain four linear algebraic equations for unknowns α_M that can be written in matrix form as

$$(2.14) \qquad C\alpha_M^\top = \omega\alpha_M^\top,$$

where the superscript $\top$ is the transpose operator, and the 4×4 matrix C reads

$$(2.15) \qquad C = \begin{bmatrix} \int y_0 d\boldsymbol{v} & 2\int v_1 y_0 d\boldsymbol{v} & 2\int v_2 y_0 d\boldsymbol{v} & \int V y_0 d\boldsymbol{v} \\ \int v_1 y_0 d\boldsymbol{v} & 2\int v_1^2 y_0 d\boldsymbol{v} & 2\int v_1 v_2 y_0 d\boldsymbol{v} & \int v_1 V y_0 d\boldsymbol{v} \\ \int v_2 y_0 d\boldsymbol{v} & 2\int v_1 v_2 y_0 d\boldsymbol{v} & 2\int v_2^2 y_0 d\boldsymbol{v} & \int v_2 V y_0 d\boldsymbol{v} \\ \int V y_0 d\boldsymbol{v} & 2\int V v_1 y_0 d\boldsymbol{v} & 2\int V v_2 y_0 d\boldsymbol{v} & \int V^2 y_0 d\boldsymbol{v} \end{bmatrix},$$

with $V = v^2 - 1$ and

$$(2.16) \qquad y_0(\boldsymbol{v}) = \frac{E(\boldsymbol{v})}{1 + iK\boldsymbol{\theta} \cdot \boldsymbol{v}}.$$

In general, the value of ω can be obtained by numerically computing the eigenvalues ω of matrix C. The magnitude of the largest eigenvalue, i.e., the spectral radius, is the convergence rate. The result of spectral radius as a function of the Knudsen number is shown in Figure 1. Specifically, when $K \to 0$, we find (see Appendix A) that the spectral radius can be calculated analytically as

$$(2.17) \qquad \omega_{CIS} = 1 - \frac{K^2}{2} + O(K^3).$$

The fact that ω_{CIS} approaches one when $K \to 0$ means that errors defined in (2.8) and (2.10) decay rather slowly. Worse yet, the CIS encounters the problem of "false

convergence." According to the analysis of Adam and Larsen for the radiation transfer equation [1] (similarly for the BGK equation here), if the iteration is terminated at the $(k+1)$-th step with the convergence criterion

$$(2.18) \qquad |\Phi_M^{(k+1)} - \Phi_M^{(k)}| < \epsilon,$$

then the relative difference from the true steady-state solution Φ_M of (2.1) is estimated as

$$(2.19) \qquad |\Phi_M^{(k+1)} - \Phi_M| < \frac{\omega_{CIS}}{1 - \omega_{CIS}}\epsilon \to \frac{2\epsilon}{K^2} \quad \text{when } K \to 0.$$

The asymptotic expression (2.17) at $K \to 0$ shows that, if the convergence criterion is chosen as (2.18), the error in the final iteration can be much larger than the pre-assigned value ϵ; thus false convergence occurs if ϵ is not small enough. To reach the same convergence criterion for $|\Phi_M^{(k+1)} - \Phi_M|$, the total number of iterations must scale as $O(K^{-N})$ with $N > 2$. This proves that in CIS it is very hard to obtain the converged solution in the near-continuum flow regime; one numerical example is given in Figure 3 of [25].

3. GSIS and its convergence rate. In GSIS, additional macroscopic equations are coupled with CIS to boost convergence [22]. The algorithm is summarized below. First, given the value of velocity distribution function $h^{(k)}(\boldsymbol{x}, \boldsymbol{v})$ at the kth iteration step, the velocity distribution function at the intermediate $(k+1/2)$th step is obtained by solving the following kinetic equation:

$$(3.1) \qquad h^{(k+1/2)} + K\boldsymbol{v} \cdot \frac{\partial h^{(k+1/2)}}{\partial \boldsymbol{x}} = h_{eq}(h^{(k)}).$$

Second, macroscopic quantities $\bar{M} = (\bar{\varrho}, \bar{u}_1, \bar{u}_2, \bar{\tau})$ are introduced to update M at the (k+1)th iteration step in the following manner,

$$(3.2) \qquad M^{(k+1)} = \beta\bar{M} + (1 - \beta)M^{(k+1/2)},$$

where $0 \leq \beta \leq 1$ is the relaxation coefficient: when $\beta = 0$, the scheme is reduced to the CIS with no fast convergence at small Knudsen numbers. The macroscopic quantities $\bar{M}$ at the $(k + 1)$th iteration step can be obtained by solving the partial differential equations (note that the Einstein summation is used)

$$(3.3) \qquad \frac{\partial \bar{u}_i}{\partial x_i} = 0,$$

$$(3.4) \qquad \frac{\partial \bar{\varrho}}{\partial x_i} + \frac{\partial \bar{\tau}}{\partial x_i} + \frac{\partial \bar{\sigma}_{ij}}{\partial x_j} = 0,$$

$$(3.5) \qquad \frac{\partial \bar{q}_i}{\partial x_i} = 0,$$

which are obtained by taking the velocity moments of the BGK equation (2.1). However, in GSIS the shear stress $\bar{\sigma}_{ij}$ and heat flux $\bar{q}_i$ are not directly calculated from the velocity distribution function $h^{(k+1/2)}$ according to (2.4) and (2.5) but are reconstructed as

$$(3.6) \qquad \bar{\sigma}_{ij} = -2K_e \frac{\partial \bar{u}_{<i}}{\partial x_{j>}} + \text{HoT}_{\sigma_{ij}},$$

$$(3.7) \qquad \bar{q}_i = -K_e \frac{\partial \bar{\tau}}{\partial x_i} + \text{HoT}_{q_i},$$

such that (3.3), (3.4), and (3.5) are reduced to the linearized Navier–Stokes equations when the high-order terms $\mathrm{HoT}_{\sigma_{ij}}$ and HoT_{q_i} vanish and when K_e takes the value of K; the role of K_e will be discussed below in section 3.3, where we will show the inclusion of the Newton's law for shear stress, and the Fourier's law for heat conduction in (3.6) and (3.7) is critical to realizing the fast convergence in the near-continuum flow regime. Note that the high-order terms $\mathrm{HoT}_{\sigma_{ij}}$ and HoT_{q_i} should be derived exactly from the kinetic equation (2.1), so that the rarefaction effects beyond the Navier–Stokes level are all captured.

There are many ways to construct the expressions for these high-order terms. In our paper [22], they are constructed by multiplying (2.1) with $\left(v_i v_j - v^2 \delta_{ij}/2\right) E$ and $v_i \left(v^2 - 2\right) E$, respectively, and integrating the resultant equations with respect to the molecular velocity $\boldsymbol{v}$:

$$(3.8) \qquad \mathrm{HoT}_{\sigma_{ij}} = 2K_e \frac{\partial u_{<i}^{(k+1/2)}}{\partial x_{j>}} - 2K \int \left(v_i v_j - \frac{v^2}{2}\delta_{ij}\right)\boldsymbol{v} \cdot \frac{\partial h^{(k+1/2)}}{\partial \boldsymbol{x}}d\boldsymbol{v},$$

$$(3.9) \qquad \mathrm{HoT}_{q_i} = K_e \frac{\partial \tau^{(k+1/2)}}{\partial x_i} - K \int v_i(v^2 - 2)\boldsymbol{v} \cdot \frac{\partial h^{(k+1/2)}}{\partial \boldsymbol{x}}d\boldsymbol{v}.$$

Clearly, the above high-order terms are correct when the steady state is reached. However, during iteration when the steady state is not reached, (3.6) and (3.7) are not correct since macroscopic quantities $\bar{M}$ are evaluated at the $(k+1)$th iteration step, while high-order terms $\mathrm{HoT}_{\sigma_{ij}}$ and HoT_{q_i} are computed using the intermediate velocity distribution function at the $(k+1/2)$th iteration step.

3.1. The case of $\beta = 1$ and $K_e = K$. To calculate the convergence rate of GSIS, we introduce the error function for the velocity distribution function as

$$(3.10) \qquad Y^{(k+1/2)}(\boldsymbol{x}, \boldsymbol{v}) = h^{(k+1/2)}(\boldsymbol{x}, \boldsymbol{v}) - h^{(k)}(\boldsymbol{x}, \boldsymbol{v}) = \omega^k y(\boldsymbol{v})\exp(i\boldsymbol{\theta} \cdot \boldsymbol{x}),$$

while the error functions Φ_M are still defined as $\Phi_M^{(k+1)}(\boldsymbol{x}) = M^{(k+1)}(\boldsymbol{x}) - M^{(k)}(\boldsymbol{x})$. It is clear that, according to (3.1), the solution of $y(\boldsymbol{v})$ is still given by (2.13). It should be emphasized that in GSIS, the error functions Φ_M are not directly calculated from Y but are calculated from the macroscopic synthetic equations; the equations for $\Phi_M^{(k+1)}(\boldsymbol{x})$ are given by (3.3)–(3.9) if $\bar{\varrho}, \bar{u}_1, \bar{u}_2$, and $\bar{\tau}$ are replaced by $\Phi_\varrho^{(k+1)}$, $\Phi_{u_1}^{(k+1)}$, $\Phi_{u_2}^{(k+1)}$, and $\Phi_\tau^{(k+1)}$, respectively, and $h(\boldsymbol{x}, \boldsymbol{v})$ is replaced by $Y(\boldsymbol{x}, \boldsymbol{v})$.

On substituting (3.10), (2.10), and (2.12) into the governing equations for $\Phi_M^{(k+1)}(\boldsymbol{x})$, we obtain the four linear algebraic equations,

$$(3.11) \qquad \omega(i\theta_1 \alpha_{u_1} + i\theta_2 \alpha_{u_2}) = 0,$$

$$(3.12) \qquad \omega[i\theta_1(\alpha_\varrho + \alpha_\tau) + K_e \alpha_{u_1}] = S_1,$$

$$(3.13) \qquad \omega[i\theta_2(\alpha_\varrho + \alpha_\tau) + K_e \alpha_{u_2}] = S_2,$$

$$(3.14) \qquad \omega K_e \alpha_\tau = S_\tau,$$

where the source terms, due to high-order terms in (3.8) and (3.9), are also linear functions of α_M: $S_1 = \int s_1 yE d\boldsymbol{v}$, $S_2 = \int s_2 yE d\boldsymbol{v}$, and $S_\tau = \int s_\tau yE d\boldsymbol{v}$, with

$$(3.15) \qquad s_1 = K_e v_1 + K(i\theta_1 v_1 + i\theta_2 v_2)\left[i\theta_1(v_1^2 - v_2^2) + 2i\theta_2 v_1 v_2\right],$$

$$(3.16) \qquad s_2 = K_e v_2 + K(i\theta_1 v_1 + i\theta_2 v_2)\left[2i\theta_1 v_1 v_2 + i\theta_2(v_2^2 - v_1^2)\right],$$

$$(3.17) \qquad s_\tau = K_e(v^2 - 1) + K(i\theta_1 v_1 + i\theta_2 v_2)(i\theta_1 v_1 + i\theta_2 v_2)(v^2 - 2).$$

The spectral radius of GSIS can be obtained by solving (3.11)–(3.17). That is, these equations are first rewritten in the matrix form as

$$(3.18) \qquad L\omega\alpha_M^\top = R\alpha_M^\top,$$

where the 4×4 matrix L is obtained from the left-hand side of (3.11)–(3.14) as

$$(3.19) \qquad L = \begin{bmatrix} 0 & i\theta_1 & i\theta_2 & 0 \\ i\theta_1 & K_e & 0 & i\theta_1 \\ i\theta_2 & 0 & K_e & i\theta_2 \\ 0 & 0 & 0 & K_e \end{bmatrix},$$

and due to the fact that $y(\boldsymbol{v})$ in (2.13) is a linear combination of $\alpha_\varrho, \alpha_{u_1}, \alpha_{u_2}$, and α_τ, the 4×4 matrix R is obtained from (3.15)–(3.17) as

$$(3.20) \qquad R = \begin{bmatrix} 0 & 0 & 0 & 0 \\ \int y_0 s_1 d\boldsymbol{v} & 2\int v_1 y_0 s_1 d\boldsymbol{v} & 2\int v_2 y_0 s_1 d\boldsymbol{v} & \int V y_0 s_1 d\boldsymbol{v} \\ \int y_0 s_2 d\boldsymbol{v} & 2\int v_1 y_0 s_2 d\boldsymbol{v} & 2\int v_2 y_0 s_2 d\boldsymbol{v} & \int V y_0 s_2 d\boldsymbol{v} \\ \int y_0 s_\tau d\boldsymbol{v} & 2\int v_1 y_0 s_\tau d\boldsymbol{v} & 2\int v_2 y_0 s_\tau d\boldsymbol{v} & \int V y_0 s_\tau d\boldsymbol{v} \end{bmatrix}.$$

By introducing

$$(3.21) \qquad G = L^{-1}R$$

and numerically computing the eigenvalues of the matrix G, we obtain the spectral radius ω of GSIS. The results are shown as the dotted black line in Figure 1. Specifically (see Appendix B), we find the following analytical expression for ω when $K \to 0$:

$$(3.22) \qquad \omega = \left(1 + \frac{3}{2\sqrt{2}}\right) K^2 \approx 2.06 K^2.$$

This demonstrates that the GSIS is able to boost convergence significantly in the near-continuum flow regime. However, the spectral radius increases to one when $K \to \infty$. This stands in sharp contrast to DSA schemes for rarefied Poiseuille-type flows, where the flow velocity (only in one direction) is perpendicular to spatial variables [24]. As a consequence, the synthetic equation for the only flow velocity is of diffusion type [24, 27, 19], and the spectral radius goes to zero when $K \to \infty$ and $K \to 0$. However, in GSIS we have multiple flow velocities, whose directions are inside the spatial domain, and the synthetic equations contain the continuity equation (3.3), which is not of diffusion type. Comparing GSIS with DSA, the continuity equation might be the reason why the spectral radius goes to one at large Knudsen numbers. This problem is fixed below.

3.2. The case of $\beta < 1$ and $K_e = K$. To make the spectral radius in GSIS go to zero at large Knudsen numbers, the relaxation coefficient in (3.2) is chosen as

$$(3.23) \qquad \beta = \frac{\min(K, K_{th})}{K},$$

where K_{th} is the threshold Knudsen number, so that GSIS is reduced to CIS when K is much larger than K_{th}, where the spectral radius approaches zero. Mathematically,

the spectral radius of this GSIS can be obtained by computing the eigenvalue of the matrix

$$(3.24) \qquad\qquad G = \beta L^{-1} R + (1 - \beta) C,$$

where the results at the threshold Knudsen numbers of values 1 and 4 are shown in Figure 1(a). Clearly, by choosing an approximate value of β (or K_{th}), we can make the maximum value of ω less than 0.5; from Figure 1(b) we see that the range for K_{th} is broad, i.e., it can vary from 0.5 to 4. This means that after 10 iterations, the error will be decreased by three orders of magnitude. Thus, theoretically, GSIS permits fast convergence in the whole range of the Knudsen number, which has been demonstrated by the numerical examples in our recent paper [22].

In addition to the fast convergence at large Knudsen numbers, (3.23) with $\beta < 1$ can make the algorithm more stable. This is because, when K is large, high-order terms defined in (3.8) and (3.9) may have strong variations around sharp (i.e., rectangular) corners, which leads to unphysical variations of density, velocity, and temperature when solving (3.3), (3.4), and (3.5). By updating the macroscopic quantities according to (3.2), the error at sharp boundaries is reduced, and a stable algorithm is guaranteed [22].

3.3. Why the Navier–Stokes constitutive relations important. Note that when the Knudsen number is small, we choose $\beta = 1$ in (3.2) and $K_e = K$ in (3.6) and (3.7); this means that in the near-continuum regime, the constitutive relations in the Navier–Stokes equations, i.e., the Newton's law for shear stress and the Fourier's law for heat conduction, are explicitly included in the macroscopic synthetic equations. This turns out to be extremely important for the fast convergence of GSIS, as the spectral radius goes to zero when $K \to 0$; see Figure 1 and (3.22).

To demonstrate this superiority, we calculate the spectral radius ω by choosing different values of K_e when the Knudsen number K is small; the results in Figure 2 show that only when $K_e = K$ can the spectral radius go to zero when $K \to 0$. Moreover, when $K < 0.2$, the further K_e deviates from K, the larger the spectral radius and hence the slower the convergence. When K_e deviates too much from K, say $K_e = 0.45K$, ω can be even larger than one, which means that the GSIS is unstable. In the extreme case $K_e/K \to 0$, from the numerical solutions we find that $\omega \to K/K_e$. These results confirm that the fastest convergence can be realized by including the Navier–Stokes constitutive relations explicitly in the macroscopic synthetic equations. The secret to the fast convergence of GSIS is that (3.3), (3.4), and (3.5) are exactly the linearized Navier–Stokes equations of the corresponding linearized kinetic equation when higher-order terms are neglected, which leads to diffusion equations for the flow velocity and temperature; these diffusion equations enable efficient flow information exchange across the whole computational domain. If the shear stress and heat flux in (3.4) and (3.5) are directly computed from the $h^{(k+1/2)}$ according to (2.4) and (2.5), there are no diffusion equations for the velocity and temperature.

4. Asymptotic preserving property of GSIS. Note that in GSIS the kinetic equation and the macroscopic synthetic equations can be solved by different numerical methods with different orders of accuracy. Now we consider the influence of spatial discretization in the gas kinetic solver on the accuracy of GSIS, based on the assumptions that (i) synthetic equations can be solved exactly, and (ii) the spatial cell size Δx is able to capture the physical solution of the Navier–Stokes equations. To this
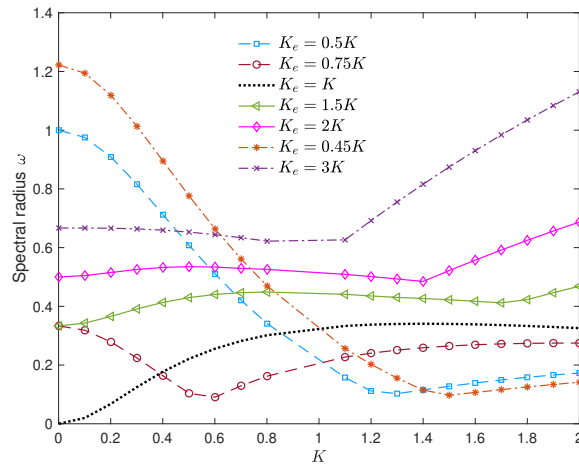
FIG. 2. *The spectral radius ω as a function of the Knudsen number K in GSIS when K_e in (3.6) and (3.7) takes different values and the relaxation coefficient in (3.2) is $\beta = 1$.*

end, we consider whether the Navier–Stokes equations can be derived, through the Chapman–Enskog expansion [4], from the discretized gas kinetic equation with the following scaling:

$$\Delta x \sim K^{1/\alpha}. \tag{4.1}$$

Here α denotes the order of accuracy in the asymptotic preserving of the Navier–Stokes equations. Clearly, the larger the value of α, the better the numerical scheme, as we can use fewer spatial cells to achieve the same accuracy. It has been rigorously proven that the discrete unified gas kinetic scheme has $\alpha = 2$, so that Δx can be much larger than the mean free path to capture the hydrodynamics in bulk regions [10]. If $\alpha = \infty$, the scheme will capture the hydrodynamical behavior of gas when Δx is approximately the system size (no matter the value of K), as long as this size is adequate for capturing the flow physics, for example, the dynamics of a sound wave whose wavelength is approximately the system size.

Since the spectral radius of GSIS approaches zero when $K \to 0$, the converged solution can be found within a few iterations, and we have $h_{eq}^{(k+1)} = h_{eq}^{(k)}$ and $M^{(k+1)} = M^{(k)}$. Thus, when the iteration is converged, the kinetic equation (3.1) in the discretized form can be written as

$$\boldsymbol{v} \cdot \frac{\partial h}{\partial \boldsymbol{x}} + O(\Delta x^n)\delta(h) = \frac{h_{eq} - h}{K}, \tag{4.2}$$

where n is the order of approximation for the spatial derivative $\partial h/\partial x$, and $\delta(h)$ is the $(n+1)$th order derivative of h. For instance, if we use the second-order upwind finite difference scheme, we have $n = 2$. If the third-order approximating polynomials are used in the DG method [21, 20], we have $n = 4$.

In the Chapman–Enskog expansion, the velocity distribution function is approximated by the Taylor expansion $h = h_0 + Kh_1 + \cdots$. By subsisting this expansion into (4.2) and collecting terms with the order of K^{-1}, we have $h_0 = f_{eq}$ when the following largest scaling is chosen:

$$\Delta x \sim K^{1/\infty} = O(1). \tag{4.3}$$

Under the scaling (4.3), by collecting terms with the order K^0, we have $h_1 = -\boldsymbol{v} \cdot \partial h_{eq}/\partial \boldsymbol{x} - \delta(h_{eq})$. Note that at small values of K we have $\beta = 1$ in (3.23) and (3.2). Thus, according to (3.6), (3.7), (3.8), and (3.9), the Newton's law for shear stress and the Fourier's law for heat conduction are recovered in the macroscopic synthetic equations with accuracy $O(K^2)$:

$$(4.4) \qquad \sigma_{ij} = -2K\frac{\partial u_{<i}}{\partial x_{j>}} + O(K^2), \quad q_i = -K\frac{\partial \tau}{\partial x_i} + O(K^2).$$

Thus, as long as the spatial resolution $\Delta x = O(1)$ is able to capture the physical solution of the Navier–Stokes equations, GSIS is able to recover the linearized Navier–Stokes equations when $K \to 0$; in this sense the GSIS is better than the discrete unified gas kinetic scheme [10] where $\Delta x = O(\sqrt{K})$. Therefore, the overall order of accuracy of GSIS depends only on the order for solving the macroscopic synthetic equations, that is, n in (4.2). In reality, however, such a large spatial cell size $\Delta x = O(1)$ cannot be used in regions with Knudsen layers or shock structures, where the physical solutions require a spatial resolution of $O(K)$. Fortunately, these kinetic layers only take up a small fraction of the computational domain, say, in the vicinity of solid walls, which can be captured by implicit schemes with nonuniform spatial discretization. This will be tested in the following numerical examples.

5. Numerical examples. To assess the analytical results in the previous sections, we simulate the one-dimensional coherent Rayleigh–Brillouin scattering, sound wave propagation, and Couette flows, as well as the two-dimensional thermal edge flow.

5.1. Coherent Rayleigh–Brillouin scattering. In coherent Rayleigh–Brillouin scattering, the wavelike density perturbation in gas is created by a moving optical lattice, where the governing equation for the velocity distribution function h' can be written as

$$(5.1) \qquad \frac{\partial h'}{\partial t} + v_2\frac{\partial h'}{\partial x_2} = \frac{h'_{eq} - h'}{K} + 2v_2\cos(2\pi x_2 + 2\pi f_s t),$$

where f_s is the frequency of the moving optical lattice; we choose $f_s = \sqrt{5/6}$ (i.e., the sound speed normalized by the most probable speed of gas molecules) so that the amplitude of perturbed density will scale as $1/K$ when the Knudsen number is small. If the numerical scheme cannot preserve the Navier–Stokes limit when $K \to 0$, then a huge number of spatial cells is needed to keep a low numerical dissipation; otherwise, the amplitude will be much smaller than the converged solution; see Figure 3(b) and Figure 4 below. Since the interaction between the gas and solid wall is absent [26], this problem is ideal for testing the accuracy and efficiency of the kinetic scheme.

The problem is periodic in both temporal and spatial directions. Therefore, using the transform $h'(x_2, \boldsymbol{v}, t) = h(x_2, \boldsymbol{v})\exp(2\pi i f_s t)$, the final perturbed density profile can be obtained by solving the equation [26]

$$(5.2) \qquad 2\pi i f_s h + v_2\frac{\partial h}{\partial x_2} = \frac{h_{eq} - h}{K} + 2v_2\cos(2\pi x_2),$$

which can be handled by implicit solvers.

Note that in order to keep the calculation more realistic, in the following the linearized Shakhov kinetic model is used, and the velocity distribution function contains

the three-dimensional molecular velocity space [16]. That is, the reference distribution function in (5.2) now becomes

$$(5.3) \qquad h_{eq}(\boldsymbol{x}, \boldsymbol{v}) = \varrho(\boldsymbol{x}) + 2\boldsymbol{u}(\boldsymbol{x}) \cdot \boldsymbol{v} + \tau(\boldsymbol{x})\left(v^2 - \frac{3}{2}\right) + \frac{4}{15}\boldsymbol{q}(\boldsymbol{x}) \cdot \boldsymbol{v}\left(v^2 - \frac{5}{2}\right),$$

where the perturbed density is $\varrho = \int E_3(\boldsymbol{v})h d\boldsymbol{v}$, with the equilibrium velocity distribution function $E_3(\boldsymbol{v}) = \exp(-v^2)/\pi^{1.5}$, the flow velocity is $\boldsymbol{u} = \int \boldsymbol{v}E_3(\boldsymbol{v})h d\boldsymbol{v}$, the perturbed temperature is $\tau = \int(2v^2/3 - 1)E_3(\boldsymbol{v})h d\boldsymbol{v}$, and the heat flux is $\boldsymbol{q} = \int \boldsymbol{v}\left(v^2 - 5/2\right)E_3(\boldsymbol{v})h d\boldsymbol{v}$.

The presence of the first term in (5.2) modifies the synthetic equations (3.3), (3.4), and (3.5) to the forms [22]

$$(5.4) \qquad 2\pi i f_s \bar{\varrho} + \frac{\partial \bar{u}_i}{\partial x_i} = 0,$$

$$(5.5) \qquad 2\pi i f_s \bar{u}_i + \frac{\partial \bar{\varrho}}{\partial x_i} + \frac{\partial \bar{\tau}}{\partial x_i} + \frac{\partial \bar{\sigma}_{ij}}{\partial x_j} = 0,$$

$$(5.6) \qquad 2\pi i f_s \bar{\tau} + \frac{\partial \bar{q}_i}{\partial x_i} + \frac{\partial \bar{u}_i}{\partial x_i} = 0,$$

while the shear stress and heat flux are modified into the following forms:

$$(5.7) \qquad 2\pi i f_s \sigma_{22} + \mathrm{HoT}_{\sigma_{22}} + \frac{4}{3}\frac{\partial \bar{u}_2}{\partial x_2} = -\delta_{\mathrm{rp}}\sigma_{22},$$

$$(5.8) \qquad 2\pi i f_s q_2 + \mathrm{HoT}_{q_2} + \frac{5}{4}\frac{\partial \bar{\tau}}{\partial x_2} = -\frac{2}{3}\delta_{\mathrm{rp}}q_2.$$

Note that, after obtaining $h^{(k+1/2)}$ from the kinetic equation and $\bar{M}$ from the synthetic equations, GSIS updates $h^{(k+1)}$ by the following formula:

$$(5.9) \qquad \begin{aligned} h^{(k+1)} = h^{(k+1/2)} + \beta\bigg[&\left(\bar{\varrho} - \varrho^{(k+1/2)}\right) + 2\left(\bar{\boldsymbol{u}} - \boldsymbol{u}^{(k+1/2)}\right) \cdot \boldsymbol{v} \\ &+ \left(\bar{\tau} - \tau^{(k+1/2)}\right)\left(v^2 - \frac{3}{2}\right)\bigg], \end{aligned}$$

such that (3.2) holds.

The comparison between CIS and GSIS in terms of efficiency and accuracy is shown in Figure 3 for the case when the Knudsen number is $K = 0.005$ and the synthetic equations in GSIS are solved by the Fourier spectral method exactly. Due to the small value of convergence rate ω, GSIS yields a converged solution even after only three iterations and when $\epsilon = 10^{-3}$, which is consistent with the analytical solution (2.19). That is,

$$(5.10) \qquad |\Phi_M^{(k+1)} - \Phi_M| < \frac{\omega_{GSIS}}{1 - \omega_{GSIS}}\epsilon \to \epsilon K^2 \quad \text{when } K \to 0.$$

However, since ω_{CIS} approaches one when $K \to 0$, CIS needs a huge number of iterations, and the convergence criterion has to be set very small, i.e., $\epsilon = 10^{-10}$ in this case. This is also consistent with the prediction in (2.19).

In terms of spatial accuracy, Figure 3(b) shows that GSIS can asymptotically preserve the Navier–Stokes limit with $\Delta x \sim O(1)$ provided this spatial resolution is adequate for describing the physical problem (here it is the density wave profile),
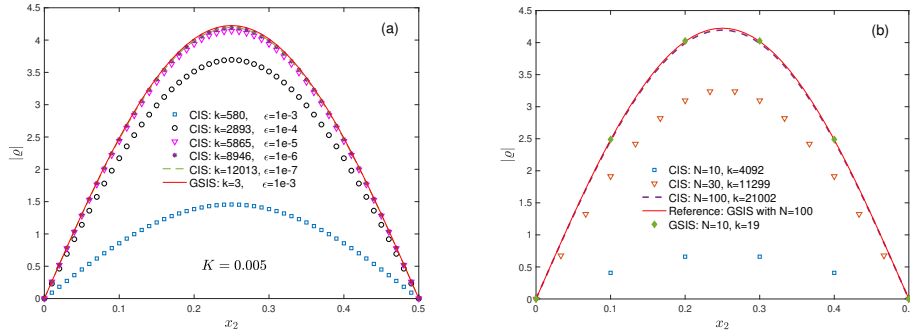
FIG. 3. *Comparisons of the density profile in coherent Rayleigh–Brillouin scattering obtained from CIS and GSIS when the Knudsen number is $K = 0.005$. (a) The convergence history of CIS at different values of the error $\epsilon = \left| \int |\varrho^{(k+1)} dx_2| / \int |\varrho^{(k)}| dx_2 - 1 \right|$. The spatial region $x_2 \in [0,1]$ is divided into $N = 100$ uniform cells, and due to symmetry only half of the density wave profile is plotted. The result from GSIS is converged even when $\epsilon = 10^{-3}$ after three iterations. (b) The influence of spatial cell number on the density profile, where the iteration is terminated when $\epsilon < 10^{-10}$. The kinetic equation is solved by the second-order upwind finite difference, while the synthetic equations are solved by the Fourier spectral method.*

while the CIS needs a much smaller spatial cell size in order to keep the numerical dissipation small: when the cell size is large, the numerical dissipation leads to a smaller amplitude of the density wave compared to the true solution due to the strong numerical dissipation.

To further show the importance of spatial resolution, in Figure 4 we consider the same problem when the Knudsen number is $K = 10^{-8}$. Even in this case the Euler equation cannot be used; otherwise, the amplitude of perturbation will go to infinity. The extremely small value of K poses a real challenge to the kinetic scheme, as any small value of numerical dissipation could easily contaminate the final solution, which leads to a significantly smaller amplitude of density perturbation. Even at such a small Knudsen number, if the macroscopic equation is solved exactly (by the Fourier spectral method) and $\Delta x \sim O(1)$ is able to capture the spatial variation, GSIS has an infinite order of accuracy; see the circles in Figure 4. However, when the second-order finite difference scheme is used to solve the synthetic equations, we need more than 2000 spatial points to capture the density perturbation; this is understandable since the numerical dissipation (or numerical viscosity) $(\Delta x)^2 = 2.5 \times 10^{-7}$ is larger than the physical viscosity (here it is reflected by the Knudsen number K). When the synthetic equations are solved by the fourth-order finite difference method, we see that $N = 100$ leads to wrong solutions, while $N = 300$ yields an accurate solution. This is because the numerical dissipations are about $(\Delta x)^4 = 10^{-8}$ and 1.2×10^{-10}, respectively, so that the former is too dissipative while the latter is accurate.

5.2. Sound wave propagation. The governing equation in this problem is the same as that in coherent Rayleigh–Brillouin scattering, except here we have no external driving force, and the diffuse boundary condition is imposed on two walls: the one at $x_2 = 0$ is oscillating in the x_2 direction with a velocity $u_2 = \cos(2\pi f_s t)$ while the other at $x_2 = 1$ is stationary; see the schematic in Figure 5. The detailed
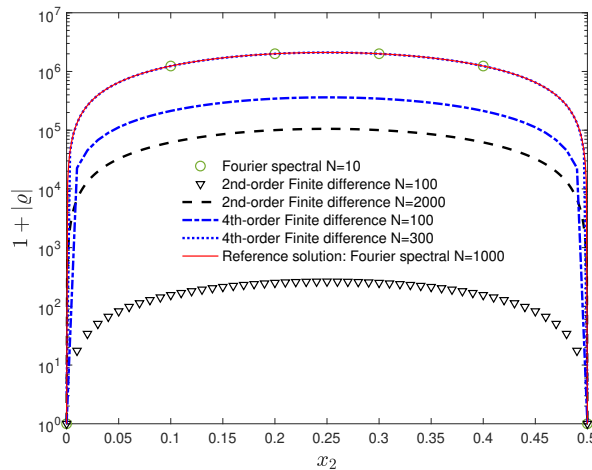
FIG. 4. *Comparisons of the density profile in coherent Rayleigh–Brillouin scattering, where the kinetic equation is solved by the second-order upwind finite difference, while the macroscopic equations are solved by various schemes with different numbers of spatial points (N). The Knudsen number is $K = 10^{-8}$. The density amplitude is shifted by one in order to show it in the log scale.*

form of the diffuse boundary condition for the specific problem is [22]

$$\text{(5.11)} \quad \begin{aligned} h\left(x_2 = 0, \boldsymbol{v}\right) &= \sqrt{\pi} + 2v_2 - 2\sqrt{\pi} \int_{v_2 < 0} v_2 h\left(x_2 = 0, \boldsymbol{v}\right) \mathrm{d}\boldsymbol{v} \quad \text{when } v_2 > 0, \\ h\left(x_2 = 1, \boldsymbol{v}\right) &= 2\sqrt{\pi} \int_{v_2 > 0} v_2 h\left(x_2 = 1, \boldsymbol{v}\right) \mathrm{d}\boldsymbol{v} \quad \text{when } v_2 < 0. \end{aligned}$$

We choose $f_s = 1/2\pi$ and $\sqrt{\pi}K/2 = 0.001$, and the kinetic and the macroscopic equations are solved by the DG method with different orders of accuracy. This test is used to show that when the Knudsen layer near the solid walls is well resolved, the accuracy of GSIS is mainly determined by the accuracy in solving the macroscopic synthetic equations.

In the numerical simulation we assume that the thickness of the Knudsen layer is about four times the mean free path in the immediate vicinity of walls [19], which is divided into $N_\lambda = 16$ equal cells; see Figure 5(a). The bulk region $0.004 < x_2 < 0.996$ is partitioned by N_b uniform cells. The order of the DG scheme for the kinetic equation is denoted by n_K, while that for the synthetic equations is n_S. In the constitutive relations (3.6) and (3.7), we choose $K_e = K$. During iteration, the macroscopic quantities $M^{(k+1)}$ are updated based on (3.2), and the relaxation coefficient is chosen as

$$\text{(5.12)} \quad \beta = \frac{\min\left(K_\mathrm{loc}, K_{th}\right)}{K_\mathrm{loc}} \quad \text{with } K_{th} = \min\left(1, \frac{5}{n_\mathrm{K} - 1}\right),$$

where K_loc is the local Knudsen number estimated from the local cell size: $K_\mathrm{loc} = K/L_\mathrm{loc}$, with L_loc the minimum height of the triangles used in DG, where the one-dimensional problem is actually simulated on a two-dimensional domain partitioned by structured triangles, and the periodic boundary condition is imposed on the lateral boundaries of the domain. Note that the Knudsen number is defined as the mean free
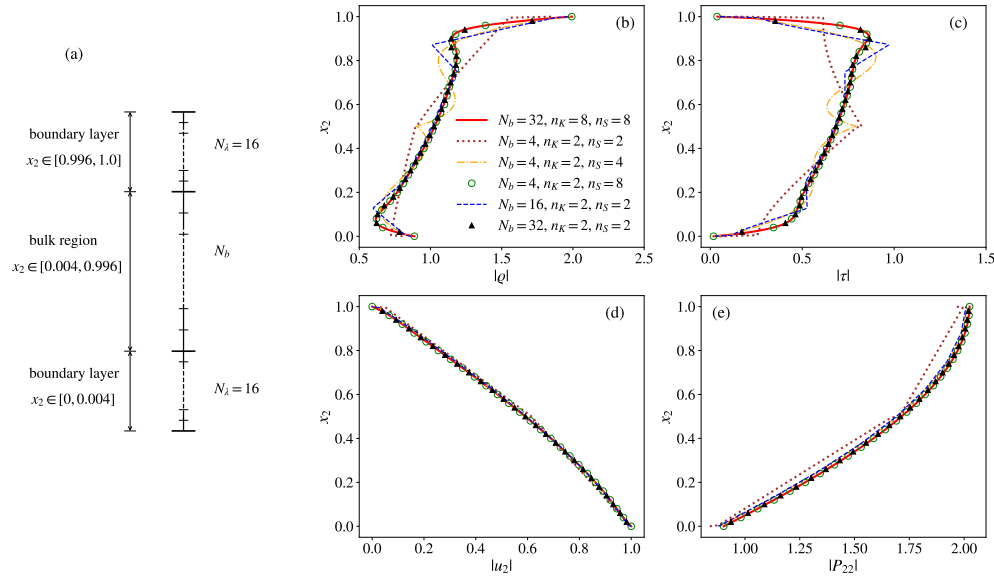
FIG. 5. *One-dimensional sound wave propagation induced by an oscillating wall at $x_2 = 0$ when the Knudsen number is $K = 0.001$. (a) Schematic illustration of the bulk region and boundary layer, and spatial discretization along x_2. (b)–(e) are, respectively, the amplitudes of density $|\varrho|$, temperature $|\tau|$, longitudinal velocity $|u_2|$, and normal pressure $|P_{22}| = |\sigma_{22} + \varrho + \tau|$ obtained from schemes with different orders of accuracy and numbers of cells.*

path over the characteristic system length L, and the spatial coordinate has been normalized by L.

Figure 5(b)–(e) shows the amplitudes of density, temperature, velocity, and normal pressure obtained from schemes with different orders of accuracy and numbers of cells. By choosing the numerical results with $N_b = 32$ and $n_K = n_S = 8$ as the reference, we see that the increase of n_S or N_b leads to solutions converging toward the reference, even when the kinetic equation is solved with second-order accuracy, i.e., $n_K = 2$. This means that in GSIS the accuracy is controlled by the macroscopic solver, at least in the near-continuum flow regime.

Table 1 shows the total number of iterations and the amplitude of normal pressure at the oscillating wall for different combinations of N_b, n_K, and n_S when ϵ defined in (2.7) is less than 10^{-5}. For all test cases, the convergence is reached within 50 iteration steps, which demonstrates the efficiency of GSIS, even when the streaming operator is discretized. The reason why the total iteration step is larger than that in the coherent Rayleigh–Brillouin scattering is because, in this case, although K is small, the presence of the Knudsen layer makes $K|\boldsymbol{\theta}|$ approximately one in (2.13). Thus, a relatively large iteration number is needed. On the other hand, Table 1 further confirms that the accuracy of the solution in the bulk region is mainly determined by the accuracy in solving the macroscopic equations. As a consequence, the higher the order of DG for the macroscopic equations, the more accurate the solution. Furthermore, accurate results can be obtained once the macroscopic quantities are well resolved on a coarse mesh, where the cell size is much larger than the mean free path of gas molecules. For instance, when the eighth-order DG for the macroscopic equations is employed with $N_b = 4$, converged results are obtained on a mesh in the bulk region 248 times larger than the molecular mean free path. This is consistent with

TABLE 1

One-dimensional sound wave propagation when $\sqrt{\pi}K/2 = 0.001$. Shown are the number of iterative steps (Itr) when the residual $\epsilon < 10^{-5}$ and the amplitude of normal pressure $|P_{22}|$ at the oscillating wall ($x_2 = 0$) under different combinations of N_b, n_K, and n_S. N_b is the number of cells in the bulk region, and $L_b = 0.992/N_b$ is the cell size in the bulk region. n_K and n_S are the orders of DG for approximating the kinetic equation and synthetic equations, respectively.

| N_b | L_b | $n_\mathrm{K} = 2$ | | | | | | $n_\mathrm{K} = 8$, $n_\mathrm{S} = 8$ | |
| | | $n_\mathrm{S} = 2$ | | $n_\mathrm{S} = 4$ | | $n_\mathrm{S} = 8$ | | | |
		Itr	$|P_{22}|$	Itr	$|P_{22}|$	Itr	$|P_{22}|$	Itr	$|P_{22}|$
4	0.248	46	0.840	36	0.882	32	0.903	33	0.903
8	0.124	47	0.846	36	0.900	32	0.903	33	0.903
16	0.062	47	0.877	36	0.903	32	0.903	33	0.903
32	0.031	47	0.897	36	0.903	32	0.903	33	0.903

the result in section 4 that GSIS is able to asymptotically preserve the Navier–Stokes limit with a spatial size $\Delta x \sim O(1)$, provided this size is able to describe the physical solution.

5.3. One-dimensional Couette flow. We consider the steady Couette flow between two infinite parallel plates located at $x_2 = 0$ and $x_2 = 1$. The top plate moves along the positive x_1 axis with a velocity of $u_1 = 1$, while the bottom plate moves in the opposite direction with the same magnitude of speed. The unconfined Knudsen number is set as $\sqrt{\pi}K/2 = 0.01$. The diffuse boundary condition is imposed on the two plates. This test is used to show the importance of resolving the Knudsen layer [19].

The partition of the computational domain along the longitudinal direction (x_2) is similar to that in Figure 5(a). In order to guarantee the accuracy of resolution in the bulk region, the bulk region $x_2 \in [0.04, 0.96]$ is partitioned into $N_\mathrm{b} = 32$ uniform cells, and the synthetic equations are solved with $N_\mathrm{S} = 8$. Details on evaluating the constitutive relations in the synthetic equations and updating the macroscopic quantities at the $(k+1)$th iteration step are given in section 5.2. We are interested in the velocity gradient at the center of the domain,

$$(5.13) \qquad k_1 = \frac{\mathrm{d}u_1(x_2 = 0.5)}{\mathrm{d}x_2},$$

as well as the Knudsen layer function u_s [19],

$$(5.14) \qquad u_s(x_2) = \frac{u_\mathrm{NS}(x_2) - u_1(x_2)}{\sqrt{\pi}k_1 K/2},$$

where u_NS is the velocity in the bulk region approximated by $u_\mathrm{NS}(x_2) = k_1(x_2 - 0.5)$.

Figure 6(a) illustrates the Knudsen layer functions obtained from DG schemes with different values of n_K and N_λ. The reference result is obtained when 16 nonuniform cells in the Knudsen layer with refinement near the wall are used, where the minimum and maximum cell sizes are 0.0089 and 0.46 mean free paths, respectively; this nonuniform grid is more suitable for recovering the divergence of velocity gradient at the wall [13]. It is concluded that using very few cells and a lower-order scheme cannot predict the correct Knudsen layer function. An accurate solution can only be obtained by increasing the order of the scheme and/or the number of cells in the Knudsen layer.

Table 2 shows the number of iteration steps, the defect velocity at the wall, and the velocity gradient k_1 for different combinations of N_λ and n_K when ϵ defined in
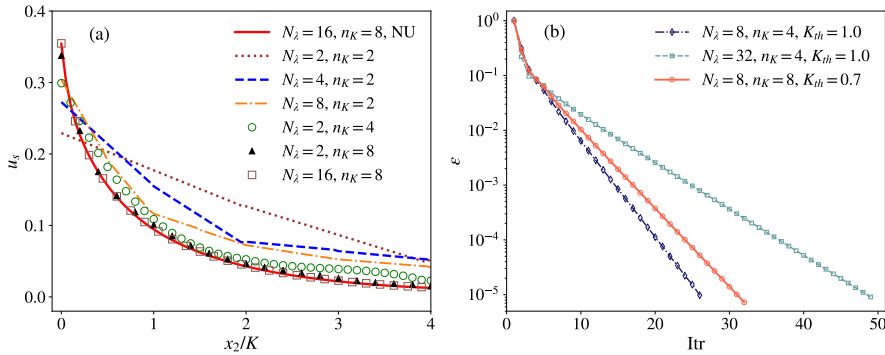
FIG. 6. (a) *The Knudsen layer functions in one-dimensional Couette flow obtained from DG schemes with different orders of accuracy n_K (for the kinetic equation) and numbers of uniform cells N_λ. The unconfined Knudsen number is $\sqrt{\pi}K/2 = 0.01$. The order of the DG scheme for the macroscopic equations is $n_S = 8$, and the bulk region is partitioned by 32 uniform cells. Note that the reference result (red solid line labeled "NU") is obtained on the grid with 16 nonuniform cells in the Knudsen layer, with refinement approaching the wall. (b) The error ϵ as a function of the iteration step. The results are obtained on the mesh of $L_\lambda = 0.16/K$ and $L_b = 128/K$.*

TABLE 2
The number of iterative steps (Itr), the defect velocity u_s at the wall, and the Knudsen layer function $k_1 = \mathrm{d}u_1(x_2 = 0.5)/\mathrm{d}x_2$ under different combinations of N_λ and n_K in one-dimensional Couette flow with $\sqrt{\pi}K/2 = 0.01$. $L_\lambda = 0.04/N_\lambda$ is the uniform cell size in the Knudsen layer. The bulk region is partitioned by 32 uniform triangles, and the order of the DG scheme for the macroscopic equations is $n_S = 8$.

N_λ	$\dfrac{L_\lambda}{\sqrt{\pi}K/2}$	$n_K = 2$			$n_K = 4$			$n_K = 8$		
		Itr	u_s	k_1	Itr	u_s	k_1	Itr	u_s	k_1
2	2.00	43	0.229	1.957	27	0.299	1.955	27	0.338	1.955
4	1.00	32	0.273	1.957	26	0.322	1.955	30	0.349	1.955
8	0.50	28	0.304	1.956	26	0.338	1.955	32	0.354	1.955
16	0.25	36	0.324	1.956	36	0.349	1.955	43	0.355	1.955
32	0.13	49	0.339	1.956	49	0.353	1.955	55	0.354	1.955
64	0.06	62	0.348	1.956	48	0.354	1.955	66	0.353	1.955

(2.7) is less than 10^{-5}. The convergence can be reached at around 30 iteration steps when the cell size in the Knudsen layer L_λ is not smaller than 0.25 mean free path. However, as the cell size further reduces, the number of iterations increases. This is due to the fact that the local Knudsen number Kn_{loc} appearing in (5.12) depends on the cell size becoming large, and the coefficient β in (3.2) for updating the macroscopic quantities is much less than one. Therefore, the macroscopic quantities are not fully corrected by the solutions from the synthetic equations, which reduces the efficiency of GSIS.

The history of error decay is plotted in Figure 6(b) for selected spatial meshes and DG resolutions, where the errors decrease by 2–3 orders of magnitude within the first 10 iterations; after that, a steeper decay rate can be seen.

It is interesting to note that even when the Knudsen layer is not resolved, the velocity gradients (5.13) in Table 2 all approach the reference value. This is understandable since according to (5.14), the error introduced by inaccurate capture of the Knudsen layer is $O(K)$, which is small compared to the wall velocity $O(1)$ in the near-continuum flow regimes. However, this case does not indicate that the capture of the Knudsen layer is not important. In thermal effects where the velocity slip induced in
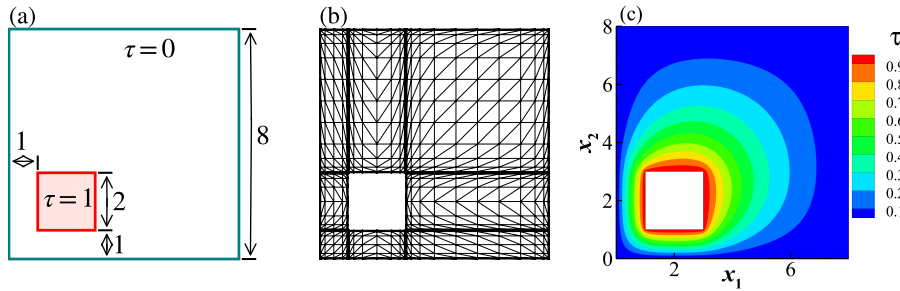
FIG. 7. *Two-dimensional thermal flow induced by a square hot beam encompassed in a cold chamber when $\sqrt{\pi}K/2 = 0.001$. Schematic illustrations of* (a) *geometry and* (b) *spatial discretization of structured triangles with refinement in the vicinity of solid walls.* (c) *Typical temperature contours obtained by DG schemes of $n_K = n_S = 6$ and on a spatial mesh of 16,104 triangles. Note that all the flow properties are symmetric about the diagonal joining the lower-left and upper-right corners of the chamber.*

the Knudsen layer is the origin of gas motion [17], the Knudsen layer must be resolved in order to obtain an accurate flow field in the whole computational domain; see the spatial discretization in [23] for an example. In the following case, we show evidence for this argument.

5.4. Two-dimensional thermal edge flow. As depicted in Figure 7(a), we consider a two-dimensional flow induced by a hot beam that is encompassed in a cold chamber. Both the beam and the chamber are square, with dimensions of 2×2 and 8×8, respectively. The beam with a (deviated) temperature of $\tau = 1$ is placed at a distance of 1 from the left and bottom walls of the enclosure. The temperature of the chamber is $\tau = 0$, and gas fills up the space between the beam and the chamber. It is well known that no bulk flow is generated at the Navier–Stokes limit, and the gas temperature is governed by the Fourier's law of heat conduction. However, under the nonequilibrium circumstances, thermal stress and thermal edge flows are induced by the rarefaction effects in the Knudsen layer [17].

We calculate the thermal flow at a challenging Knudsen number of $\sqrt{\pi}K/2 = 0.001$ when the characteristic flow length is chosen as the gap between the beam and the chamber. In addition to the fact that the physical viscosity of gas is small, the magnitude of the bulk velocity is also small; in this case high resolutions of both Knudsen layer and bulk region are necessary; otherwise, under-resolution of the Knudsen layer and/or large numerical dissipation will introduce errors at the same order as (or even larger than) that of the bulk velocity and lead to a completely wrong result.

The computational domain is partitioned by structured triangles with refinement in the vicinity of walls; see Figure 7(b), which is characterized by the total number of triangles N_Δ, the minimum cell size (the height of the local triangle) within Knudsen layer L_λ, and the maximum cell size in bulk region L_b. The diffuse boundary condition is imposed on the solid surfaces. The DG scheme is employed in the numerical simulation, and details on implementing GSIS are the same as those in the previous subsections, except here we use $K_{th} = 1$ for $n_K \leq 4$ and $K_{th} = 0.5$ for $n_K > 4$. The typical temperature fields shown in Figure 7(c) are obtained on the mesh of $N_\Delta = 16104$, $L_\lambda = 0.16K$, and $L_b = 128K$ by DG schemes with $n_K = n_S = 6$.

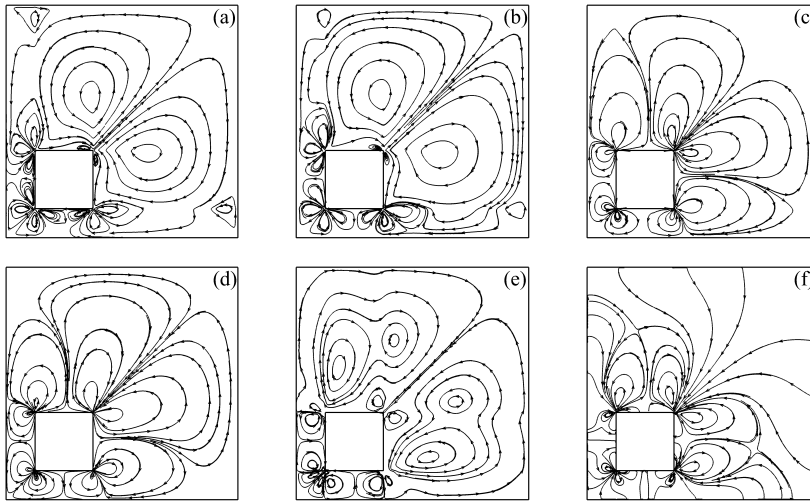We first consider the flow patterns in Figure 8, which are obtained by the DG

FIG. 8. *Streamlined patterns obtained from DG schemes with different orders of accuracy and spatial meshes in a two-dimensional thermal flow when $\sqrt{\pi}K/2 = 0.001$. (a) $L_\lambda = 0.08K$, $L_b = 128K$, and $n_K = n_S = 2$; (b) $L_\lambda = 0.04K$, $L_b = 64K$, and $n_K = n_S = 2$; (c) $L_\lambda = 0.32K$, $L_b = 256K$, and $n_K = n_S = 4$; (d) $L_\lambda = 0.08K$, $L_b = 128K$, and $n_K = n_S = 6$; (e) $L_\lambda = 0.08K$, $L_b = 128K$, $n_K = 2$, and $n_S = 6$; (f) $L_\lambda = 1.28K$, $L_b = 64K$, and $n_K = n_S = 4$.*

scheme of different orders and on different spatial meshes. On the same spatial mesh with cell size 0.08 mean free path in the Knudsen layer and 128 mean free paths in the bulk region, completely different flow patterns are obtained by second-order and sixth-order DG schemes; see Figure 8(a),(d). In the flow field predicted by the second-order scheme, four small vortices are generated around the lower-left corner of the beam, while another four are developed near the upper-right corner of the beam. At each of the lower-right and upper-left corners of the beam, three more vortices appear. Two small vortices are observed near the lower-right and upper-left corners of the chamber. On the other hand, from the sixth-order DG scheme, only eight vortices are developed, with each corner of the beam having two. Therefore, on this spatial grid ($L_\lambda = 0.08K$ and $L_b = 128K$), the second-order scheme produces larger errors; reducing the cell size by half is not adequate (see Figure 8(b)). It is also worth noting that when we only increase the order of the DG scheme for the synthetic equations, the predicted flow field is still quite different from that when the mesoscopic and the macroscopic equations are all solved using the sixth-order DG scheme; see the flow field in Figure 8(e) obtained on the mesh of $L_\lambda = 0.08K$ and $L_b = 128K$ and schemes of $n_K = 2$ and $n_S = 6$. These results show the importance of resolving the Knudsen layer, where the nonequilibrium effects are the sources of gas motion.

To further demonstrate the importance of resolving the Knudsen layer, we use the fourth-order DG scheme to solve the kinetic and synthetic equations on two different meshes: Figure 8(c) is obtained when $L_\lambda = 0.32K$ and $L_b = 256K$, while Figure 8(f) is obtained when $L_\lambda = 1.28K$ and $L_b = 64K$. Figure 8(c) shows that on the mesh where the Knudsen layer is resolved by relatively fine cells, the flow pattern with eight vortices is developed, which is very similar to the high resolution result in Figure 8(d) despite the cell size in the bulk region being relatively large. However, when the bulk region is partitioned by fine cells but the Knudsen layer is under-resolved by coarse cells, Figure 8(f) shows that although eight vortices can be observed, large errors
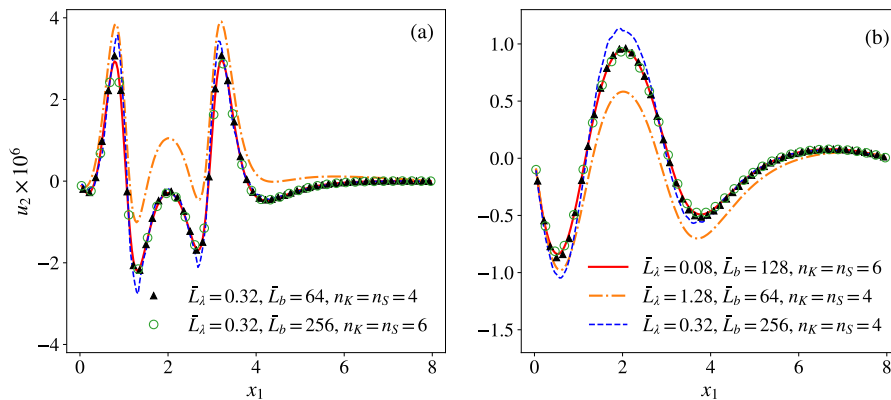
FIG. 9. *Flow velocities obtained from DG schemes with different orders of accuracy and meshes with different cell sizes in a two-dimensional thermal flow when $\sqrt{\pi}K/2 = 0.001$. (a) Vertical velocity u_2 along the horizontal line at $x_2 = 0.5$; (b) vertical velocity u_2 along the horizontal line at $x_2 = 4.5$. $\bar{L}_\lambda$ and $\bar{L}_b$ are the minimum cell size in the Knudsen layer and maximum cell size in bulk region, respectively, which are normalized by the mean free path of gas molecules, i.e. $\bar{L}_\lambda = L_\lambda/K$ and $\bar{L}_b = L_b/K$. The legends apply to both figures.*

TABLE 3

The number of iterative steps (Itr), the mean velocity magnitude $|\bar{\boldsymbol{u}}|_{x_1=0.5}$ along the horizontal line ($x_2 = 0.5$), and the computational time t_c under different combinations of spatial meshes and schemes in a two-dimensional thermal flow with $\sqrt{\pi}K/2 = 0.001$. N_Δ is the number of triangles in a mesh, L_λ is the minimum cell size (triangle height) in the Knudsen layer, and L_b is the maximum cell size in the bulk region. "Err" is the relative error of the mean velocity magnitude $|\bar{\boldsymbol{u}}|$ compared to the reference obtained with $N_\Delta = 20424$, $L_\lambda = 0.08K$, $L_b = 128K$, and $n_K = n_S = 6$. The computational time t_c is the wall time cost of each case running on eight Intel Xeon-E5-2680 CPUs using OpenMP for parallelism. Note that the molecular velocity space is discretized by 8×8 point Gauss–Hermite quadrature [18].

N_Δ	L_λ/K	L_b/K	n_K	n_S	$|\bar{\boldsymbol{u}}| \times 10^6$	Err [%]	Itr	t_c [h]
8832	0.32	256	4	4	1.072	7.4	49	0.01
16104	0.16	128	4	4	1.060	6.2	46	0.02
24864	1.28	64	4	4	1.077	7.9	45	0.06
30176	0.32	64	4	4	1.013	1.5	48	0.04
33024	0.16	64	4	4	1.013	1.5	46	0.04
8832	0.32	256	6	6	0.982	1.6	57	0.07
10400	0.16	256	6	6	0.991	0.7	55	0.12
16104	0.16	128	6	6	0.991	0.7	54	0.18
20424	0.08	128	6	6	0.998	0	60	0.21

appear near the walls, where gas seems to penetrate the solid walls.

To quantitatively show the accuracy and efficiency of numerical simulations, we plot the vertical velocity along the horizontal lines $x_2 = 0.5$ and $x_2 = 4.5$ in Figure 9. As the refinement of the spatial mesh and the increase of the order of the DG scheme, the flow properties converge to the reference ones (solid red lines) obtained on the mesh of $L_\lambda = 0.08K$ and $L_b = 128K$ and by the sixth-order DG scheme. In Table 3 we list the mean velocity along the horizontal line:

$$(5.15) \qquad\qquad |\bar{\boldsymbol{u}}| = \frac{1}{8} \int_0^8 |\boldsymbol{u}| \, (x_1, x_2 = 0.5) \, \mathrm{d}x_1.$$

The relative error between the mean velocity from the mesh of $L_\lambda = 0.08K$ and $L_b = 128K$ by the sixth-order DG scheme and the error from the mesh of $L_\lambda = 0.16K$
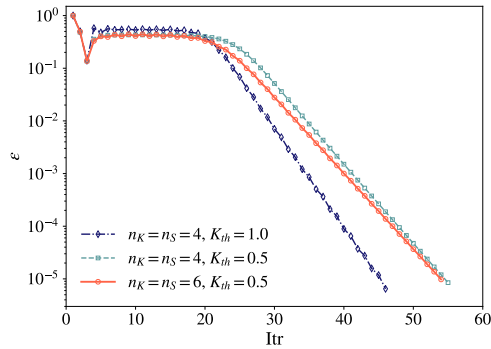
FIG. 10. *The error decay history in the two-dimensional thermal edge flow with $\sqrt{\pi}K/2 = 0.001$.*

and $L_\mathrm{b} = 256K$ by the same order scheme is within 1%, which indicates the accuracy of the reference result. The results for $|\bar{\boldsymbol{u}}|$ with different spatial discretizations and different orders of DG schemes clearly demonstrate the importance of resolving the Knudsen layer. The iteration steps and computational time cost of each case are also listed in Table 3. For all the cases, GSIS can find the steady-state solution with 50–60 steps.

We plotted the error ϵ as a function of the iteration step in Figure 10 for selected spatial meshes and DG resolutions. Compared to the Couette flow in Figure 6(b), the situation here is more complicated, where the presence of the sharp corners of the beam and the chamber leads to strong variations (probably unphysical ones) in the macroscopic quantities at the beginning of the iteration. Therefore, during the first 20 iteration steps, the error decreases slowly (and even goes up at some iteration steps). After that, however, the error declines continuously and rapidly, i.e., by two orders of magnitude within 10 iterations. The computational time for obtaining an accurate solution (with less than a 2% error in $|\bar{\boldsymbol{u}}|$ compared to the reference) can be as little as several minutes. To the best of our knowledge, no other numerical methods are able to obtain accurate results within such a short time for this kind of thermally induced flows.

6. Conclusions. In summary, based on the Fourier stability analysis, we have rigorously proven that the GSIS can lead to fast convergence of steady-state solutions. Due to the presence of the continuity equation in the macroscopic synthetic equations, the convergence property is different from other diffusion synthetic schemes for neutron transport and thermal radiation. Therefore, in GSIS the macroscopic quantities can only be partly updated according to the solution of synthetic equations when the Knudsen number is large. On the other hand, we have proven that the GSIS asymptotically preserves the Navier–Stokes limit when the spatial cell size is able to capture the physical solution; i.e., in the bulk region the spatial cell size can be $\Delta x \sim O(1)$ as long as this size is adequate for capturing the hydrodynamics. However, in the vicinity of solid walls, the physical solution requires $\Delta x \sim O(K)$ in order to capture the Knudsen layer structures. This is a disaster for explicit kinetic solvers; however, it does not pose any problems for GSIS since it is an implicit solver, so a nonuniform spatial grid can be used. These analytical results have been confirmed by several challenging numerical examples here.

It should be emphasized that GSIS has the advantage that the mesoscopic kinetic equation and the macroscopic synthetic equations can be solved by different schemes.

Since most of the cost will be spent on the kinetic solver due to additional discretization in the molecular velocity space, in multiscale simulation of rarefied gas dynamics, one can use a high-order solver for synthetic equations, while a low-order solver can be used for kinetic equations, on a coarse spatial grid, in order to save computational time and cost.

Appendix A. The spectral radius of CIS when $K \to 0$. Generally speaking, eigenvalues of the matrix C defined in (2.15) can only be calculated numerically. However, when K approaches zero, the eigenvalue can be calculated analytically. For simplicity, we take $\theta_1 = 1$ and $\theta_2 = 0$; since the problem is isotropic, any other combination of θ_1 and θ_2 with the condition $\theta_1^2 + \theta_2^2 = 1$ will lead to the same value of maximum absolute eigenvalue. In this case, (2.16) is approximated as

$$(A.1) \qquad y_0(\boldsymbol{v}) = (1 - iKv_1 - K^2 v_1^2)E(\boldsymbol{v}) + O(K^3),$$

and the matrix C can be approximated as

$$(A.2) \qquad C = \begin{bmatrix} 1 - \frac{K^2}{2} & -iK & 0 & -\frac{K^2}{2} \\ -\frac{iK}{2} & 1 - \frac{3K^2}{2} & 0 & -\frac{iK}{2} \\ 0 & 0 & 1 - \frac{K^2}{2} & 0 \\ -\frac{K^2}{2} & -iK & 0 & 1 - \frac{3K^2}{2} \end{bmatrix}.$$

The four eigenvalues of the matrix are $\omega_{1,2} = 1 - K^2/2$ and $\omega_{3,4} = 1 - 3K^2/2 \pm iK$. Therefore, the maximum absolute eigenvalue is $\omega = 1 - K^2/2$.

Appendix B. The spectral radius of GSIS when $K \to 0$. Similarly, the eigenvalue of the matrix G defined in (3.21) can be calculated analytically when K approaches zero. Again, here we choose $\theta_1 = 1$ and $\theta_2 = 0$. Also, we choose $K_e = K$; in section 3.3 we found that this leads to the smallest spectral radius when $K \to 0$. Thus, we have

$$L^{-1} = \begin{bmatrix} K & -i & 0 & -\frac{1}{K} \\ -i & 0 & 0 & 0 \\ 0 & 0 & \frac{1}{K} & 0 \\ 0 & 0 & 0 & \frac{1}{K} \end{bmatrix} \quad \text{and} \quad R = \begin{bmatrix} 0 & 0 & 0 & 0 \\ 0 & \frac{3K^3}{2} & 0 & \frac{iK^2}{2} \\ 0 & 0 & K^3 & 0 \\ \frac{K^3}{4} & \frac{iK^2}{2} & 0 & \frac{9K^3}{4} \end{bmatrix}.$$

Therefore, the matrix G is expressed as

$$(B.1) \qquad G = \begin{bmatrix} -\frac{K^2}{4} & -\frac{iK}{2} & 0 & -\frac{7K^2}{4} \\ 0 & 0 & 0 & 0 \\ 0 & 0 & K^2 & 0 \\ \frac{K^2}{4} & \frac{iK}{2} & 0 & \frac{9K^2}{4} \end{bmatrix},$$

where the four eigenvalues are $\omega_1 = 0$, $\omega_2 = K^2$, and $\omega_{3,4} = K^2(1 \pm 3/2\sqrt{2})$. The maximum absolute eigenvalue is $\omega \approx 2.06K^2$.

REFERENCES

[1] M. L. Adams and E. W. Larsen, *Fast iterative methods for discrete-ordinates particle transport calculations*, Progr. Nucl. Energy, 40 (2002), pp. 3–159.

[2] P. L. Bhatnagar, E. P. Gross, and M. Krook, *A model for collision processes in gases* I: *Small amplitude processes in charged and neutral one-component systems*, Phys. Rev., 94 (1954), pp. 511–525.

[3] G. A. Bird, *Molecular Gas Dynamics and the Direct Simulation of Gas Flows*, Oxford Science Publications, Oxford University Press, 1994.

[4] S. Chapman and T. G. Cowling, *The Mathematical Theory of Non-uniform Gases*, Cambridge University Press, 1970.

[5] G. Dimarco and L. Pareschi, *Implicit-explicit linear multistep methods for stiff kinetic equations*, SIAM J. Numer. Anal., 55 (2017), pp. 664–690, https://doi.org/10.1137/16M1063824.

[6] F. Filbet and S. Jin, *A class of asymptotic-preserving schemes for kinetic equations and related problems with stiff sources*, J. Comput. Phys., 229 (2010), pp. 7625–7649.

[7] F. Filbet and S. Jin, *An asymptotic preserving scheme for the ES-BGK model of the Boltzmann equation*, J. Sci. Comput., 46 (2011), pp. 204–224.

[8] H. Grad, *On the kinetic theory of rarefied gases*, Comm. Pure Appl. Math., 2 (1949), pp. 331–407.

[9] Z. Guo, K. Xu, and R. Wang, *Discrete unified gas kinetic scheme for all Knudsen number flows: Low-speed isothermal case*, Phys. Rev. E, 88 (2013), 033305.

[10] Z. Guo, J. Li, and K. Xu, *On Unified Preserving Properties of Kinetic Schemes*, preprint, https://arxiv.org/abs/1909.04923, 2019.

[11] M. T. Ho, L. H. Zhu, L. Wu, P. Wang, Z. L. Guo, Z. H. Li, and Y. H. Zhang, *A multi-level parallel solver for rarefied gas flows in porous media*, Comput. Phys. Commun., 234 (2019), pp. 14–25.

[12] J. W. Hu and X. X. Zhang, *On a class of implicit-explicit Runge-Kutta schemes for stiff kinetic equations preserving the Navier-Stokes limit*, J. Sci. Comput., 73 (2017), pp. 797–818.

[13] S. Jiang and L. S. Luo, *Analysis and accurate numerical solutions of the integral equation derived from the linearized BGKW equation for the steady Couette flow*, J. Comput. Phys., 316 (2016), pp. 416–434.

[14] E. W. Larsen, J. Morel, and W. F. Miller, *Asymptotic solutions of numerical transport problems in optically thick, diffusive regimes*, J. Comput. Phys., 69 (1987), pp. 283–324.

[15] L. Mieussens, *Discrete velocity models and numerical schemes for the Boltzmann-BGK equation in plane and axisymmetric geometries*, J. Comput. Phys., 162 (2000), pp. 429–466.

[16] E. M. Shakhov, *Approximate kinetic equations in rarefied gas theory*, Fluid Dyn., 3 (1968), pp. 112–115.

[17] Y. Sone, *Kinetic Theory and Fluid Dynamics*, Model. Simul. Sci. Eng. Technol., Birkhäuser Boston, Inc., 2002.

[18] W. Su, S. Lindsay, H. H. Liu, and L. Wu, *Comparative study of the discrete velocity and lattice Boltzmann methods for rarefied gas flows through irregular channels*, Phys. Rev. E, 96 (2017), 023309.

[19] W. Su, P. Wang, H. Liu, and L. Wu, *Accurate and efficient computation of the Boltzmann equation for Couette flow: Influence of intermolecular potentials on Knudsen layer function and viscous slip coefficient*, J. Comput. Phys., 378 (2019), pp. 573–590.

[20] W. Su, P. Wang, Y. Zhang, and L. Wu, *Implicit discontinuous Galerkin method for the Boltzmann equation*, J. Sci. Comput., 82 (2020), 39.

[21] W. Su, P. Wang, Y. H. Zhang, and L. Wu, *A high-order hybridizable discontinuous Galerkin method with fast convergence to steady-state solutions of the gas kinetic equation*, J. Comput. Phys., 376 (2019), pp. 973–991.

[22] W. Su, L. H. Zhu, P. Wang, Y. Zhang, and L. Wu, *Can we find steady-state solutions to multiscale rarefied gas flows within dozens of iterations?*, J. Comput. Phys., 407 (2020), 109245.

[23] S. Taguchi and K. Aoki, *Rarefied gas flow around a sharp edge induced by a temperature field*, J. Fluid Mech., 694 (2012), pp. 191–224.

[24] D. Valougeorgis and S. Naris, *Acceleration schemes of the discrete velocity method: Gaseous flows in rectangular microchannels*, SIAM J. Sci. Comput., 25 (2003), pp. 534–552, https://doi.org/10.1137/S1064827502406506.

[25] P. Wang, M. T. Ho, L. Wu, Z. Guo, and Y. Zhang, *A comparative study of discrete velocity methods for low-speed rarefied gas flows*, Comput. & Fluids, 161 (2018), pp. 33–46.

[26] L. Wu AND X.-J. Gu, *On the accuracy of macroscopic equations for linearized rarefied gas flows*, Adv. Aerodyn., 2 (2020), 2.

[27] L. Wu, J. Zhang, H. H. Liu, Y. H. Zhang, AND J. M. Reese, *A fast iterative scheme for the linearized Boltzmann equation*, J. Comput. Phys., 338 (2017), pp. 431–451.

[28] K. Xu AND J. C. Huang, *A unified gas-kinetic scheme for continuum and rarefied flows*, J. Comput. Phys., 229 (2010), pp. 7747–7764.